LETTER

https://doi.org/10.1038/s41586-018-0800-0

Greenland melt drives continuous export of methane from the ice–sheet bed

Guillaume Lamarche-Gagnon[1]*, Jemma L. Wadham[1], Barbara Sherwood Lollar[2], Sandra Arndt[3], Peer Fietzek[4], Alexander D. Beaton[5], Andrew J. Tedstone[1], Jon Telling[6], Elizabeth A. Bagshaw[7], Jon R. Hawkings[1,8,9], Tyler J. Kohler[10], Jakub D. Zarsky[10], Matthew C. Mowlem[5], Alexandre M. Anesio[11] & Marek Stibal[10]

Ice sheets are currently ignored in global methane budgets[1,2]. Although ice sheets have been proposed to contain large reserves of methane that may contribute to a rise in atmospheric methane concentration if released during periods of rapid ice retreat[3,4], no data exist on the current methane footprint of ice sheets. Here we find that subglacially produced methane is rapidly driven to the ice margin by the efficient drainage system of a subglacial catchment of the Greenland ice sheet. We report the continuous export of methane-supersaturated waters ($CH_{4(aq)}$) from the ice-sheet bed during the melt season. Pulses of high $CH_{4(aq)}$ concentration coincide with supraglacially forced subglacial flushing events, confirming a subglacial source and highlighting the influence of melt on methane export. Sustained methane fluxes over the melt season are indicative of subglacial methane reserves that exceed methane export, with an estimated 6.3 tonnes (discharge-weighted mean; range from 2.4 to 11 tonnes) of $CH_{4(aq)}$ transported laterally from the ice-sheet bed. Stable-isotope analyses reveal a microbial origin for methane, probably from a mixture of inorganic and ancient organic carbon buried beneath the ice. We show that subglacial hydrology is crucial for controlling methane fluxes from the ice sheet, with efficient drainage limiting the extent of methane oxidation[5] to about 17 per cent of methane exported. Atmospheric evasion is the main methane sink once runoff reaches the ice margin, with estimated diffusive fluxes (4.4 to 28 millimoles of CH_4 per square metre per day) rivalling that of major world rivers[6]. Overall, our results indicate that ice sheets overlie extensive, biologically active methanogenic wetlands and that high rates of methane export to the atmosphere can occur via efficient subglacial drainage pathways. Our findings suggest that such environments have been previously underappreciated and should be considered in Earth's methane budget.

The role of ice sheets in the global methane cycle depends on the ability (thermogenic or microbial) of subglacial environments to produce large quantities of methane (for example, as hydrates)[3,4,7], as well as the mechanisms responsible for methane export to the ice margin and subsequent release to the atmosphere. Subglacial methane hydrates have been suggested to currently exist beneath the Antarctic Ice Sheet in large enough quantities to raise atmospheric methane concentrations if released rapidly during deglaciation[4]. However, recent research has revealed the presence of active methane-oxidizing communities in subglacial ecosystems, suggesting the possibility of an efficient methane buffer by an active biological sink[5,8]. There is also ambiguity in the palaeo-record. New ice-core data suggest that geological methane (for example, from permafrost but also potentially of ice-sheet origin) had little effect on atmospheric methane concentrations over the Younger Dryas–Preboreal transition[9]; but previous estimates do suggest large subglacial methane releases from retreating palaeo-ice sheets of the Northern Hemisphere following the onset of the last deglaciation[10]. Confounding scenarios on the potency of sub-ice-sheet methane mostly result from the scarcity of empirical data, which are limited to point measurements in ice cores[11–13], Greenland marginal streams[5] and an Antarctic subglacial lake[8].

Here we provide direct evidence from the Greenland ice sheet (GrIS) for the existence of large subglacial methane reserves, where production is not offset by local sinks and there is net export of methane to the atmosphere during the summer melt season. We focus on a 600-km^2 catchment of the GrIS that has been extensively studied over the last decade, both in terms of ice dynamics and subglacial geochemistry (Supplementary Information 1a). Between 19 May and 13 July 2015, we deployed a CONTROS HydroC CH_4 sensor[14] (Kongsberg Maritime Contros, Germany) at a distance <2 km from the ice margin in the proglacial river of the Leverett Glacier (LG) (Supplementary Information 1a; Extended Data Fig. 1)[15,16]. Manual measurements supported sensor readings and CH_4 stable-isotope analyses ($\delta^{13}C$ and $\delta^{2}H$), and 16S rRNA gene-sequence data from LG runoff were used to infer the methane origin. A one-dimensional reaction-transport model was further applied to test for the possibility of hydrate formation beneath the ice in the catchment. Features of the study area suggest that results obtained are probably applicable to other ice-sheet catchments (Supplementary Information 1a) and are informative on a global scale, serving as a first-step assessment of subglacial methane contribution to present-day methane budgets.

Sensor measurements revealed that LG runoff was supersaturated in methane with respect to the atmosphere over the entire monitoring period (mean concentration of about 271 nM, compared with an atmospheric equilibrium concentration of about 4.5 nM) (Fig. 1). This is consistent with the high concentrations (up to about 24 μM) of methane detected in the basal regions of the GRIP, GISP2 and NGRIP ice cores[11–13], in marginal runoff from a small neighbouring Greenland glacier (about 3–83 μM)[5], and during experimental incubations of Greenland subglacial sediment[17]. Stepwise increases in methane concentrations closely followed the seasonal evolution of the subglacial drainage system, indicating the crucial role of hydrology in controlling methane export from the ice sheet. Clear differences in $CH_{4(aq)}$ concentrations were observed between (1) the early part of the season, during times of very low discharge, when the subglacial portal was completely ice-sealed and methane concentrations were low (mean concentration of about 64 nM) (Fig. 1; Supplementary Information 2b), (2) the emergence of a subglacial upwelling through the river ice in front of the LG on 1 June, which released methane-enriched waters stored over winter from the ice margin (mean concentration of about 4 μM before the melt season; see Supplementary Information 1b, Extended Data Fig. 1) and (3) the later season (from 19 June onwards), with elevated $CH_{4(aq)}$ concentrations (pulses) coincident with a series of four subglacial

[1]School of Geographical Sciences, University of Bristol, Bristol, UK. [2]Department of Earth Sciences, University of Toronto, Toronto, Ontario, Canada. [3]Department of Geoscience, Environment and Society, Université Libre de Bruxelles, Brussels, Belgium. [4]Kongsberg Maritime Contros GmbH, Kiel, Germany. [5]National Oceanography Centre, Southampton, UK. [6]School of Natural and Environmental Sciences, Newcastle University, Newcastle, UK. [7]School of Earth and Ocean Sciences, Cardiff University, Cardiff, UK. [8]National High Magnetic Field Lab and Earth, Ocean and Atmospheric Sciences, Florida State University, Tallahassee, FL, USA. [9]German Research Centre for Geosciences GFZ, Potsdam, Germany. [10]Department of Ecology, Faculty of Science, Charles University, Prague, Czechia. [11]Department of Environmental Sciences, Aarhus University, Roskilde, Denmark. *e-mail: guillaume.lg@bristol.ac.uk

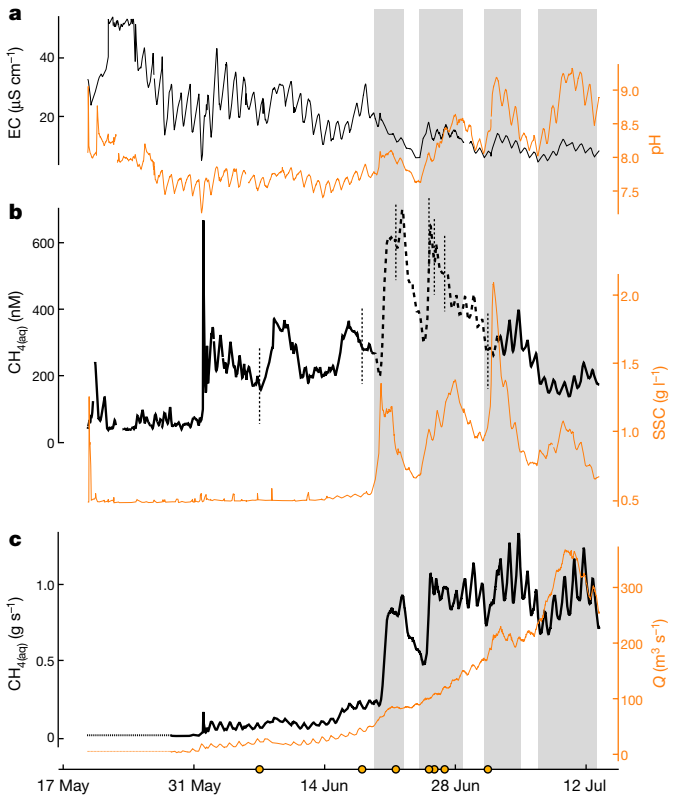

Fig. 1 | Geochemical time series of the LG proglacial river. a, Electrical conductivity (EC) and pH. **b**, $CH_{4(aq)}$ (data collected with the HydroC sensor) and suspended sediment concentrations (SSC). The dashed section corresponds to times when the HydroC sensor exhibited longer response times (see Supplementary Information 2a, Extended Data Fig. 2). Orange dots and vertical dashed lines indicate the sampling time of waters used for stable-isotope analysis (see Extended Data Table 2). **c**, $CH_{4(aq)}$ lateral flux and discharge (Q). The first data points, measured on 28 May, are extended to the first data point of the above sensor measurements (dashed horizontal lines). Abrupt increases in SSC, EC, pH and $CH_{4(aq)}$ correspond to outburst events (shaded sections) and reflect sudden drainage of sub-ice-sheet waters and sediments driven by supraglacial meltwater entering the subglacial system (Supplementary Information 2b). The left and right vertical axes correspond to the black and orange datasets, respectively.

outburst events (Supplementary Information 2b; Fig. 1). These outburst events were characterized by pulses in suspended sediment concentrations, electrical conductivity and pH (Fig. 1), indicative of subglacial origin, as previously inferred[18]. The high concentrations of $CH_{4(aq)}$ observed during these events suggest the evacuation of methane-rich subglacial waters from progressively inland sources (Supplementary Information 2b). We attribute the overall decreasing trend in methane concentration following the second outburst event to dilution by rising supraglacial ice-melt inputs to the subglacial system over the melt season. The sustained methane load observed during this period, however, indicates that subglacial methane reserves are not exhausted, despite increases in meltwater discharge (Fig. 1).

The cumulative lateral flux of $CH_{4(aq)}$ from the LG amounted to about 1.87 t (1.64–2.10 t) over the measurement period (reported ranges reflect errors in the measured concentrations and discharge; see Methods). However, we estimate that at least 2.78 t (2.43–3.12 t)—but more probably about 6.28 t (5.19–7.36 t)—of $CH_{4(aq)}$ were laterally transported at the measuring site over the entire 2015 melt season (Fig. 2; see Methods for details). Methane measurements provide conservative estimates of total methane production across the glacier, because recorded concentrations would have been influenced by oxidative and diffusive processes upstream of the measuring site and hence subglacial methane production beneath the catchment is probably larger. On the basis of previously measured microbial oxidation rates[5] and a sustained-flux scenario, we estimate that the bacterial methane sink at the LG amounted to about 1.22 t before subglacial discharge reached the ice margin, which is about 16% of the total methane export at the measuring site over the melt season (Fig. 2; Supplementary Information 2c).

We use scaling relationships between gas transfer velocities and river hydrology[19] to derive conservative approximations of diffusive fluxes of methane from the LG proglacial river. We infer that there is some evasion of methane from subglacial runoff to air spaces in subglacial channels close to the margin[20] and to the atmosphere after emergence at the glacier subglacial portal. We estimate that such atmospheric evasion constitutes the main sink of $CH_{4(aq)}$ compared to microbial oxidation, with diffusive fluxes responsible for at least 1.72 t (0.51–3.19 t) of CH_4 released to the atmosphere between the ice margin and the measuring site (Fig. 2; compared to about 0.09 t CH_4 oxidized for the same distance, or about 1% of exports; data not shown). Recent work on white-water streams has indicated that these traditionally used scaling relationships can greatly underestimate (by several orders of magnitude) diffusive fluxes in white-water systems[21,22]. Considering the high degree of turbulence observed in the LG river (Extended Data Fig. 1), we therefore stress that our estimates here constitute lower-limit values. What is clear is that the LG catchment is a source of atmospheric methane, with our minimum estimates indicating that over 18% (7.5%–26%) of exported methane reaches the atmosphere within 2 km of the ice-sheet margin.

Methane concentrations at the LG fall within the global range reported for streams and rivers (Fig. 3). A recent survey of riverine methane indeed revealed that streams have previously been overlooked as net contributors of atmospheric methane, and they are estimated to emit over 27 Tg CH_4 annually—about 15% and 40% of global wetland and lake effluxes, respectively[6]. The results presented here suggest that streams draining subglacial basins are probably no exception, with the estimated diffusive fluxes of methane at the LG falling in the higher range of reported world averages for rivers, comparable to the large fluxes observed in the Congo basin (Fig. 3, Extended Data Table 1). Because of the high uncertainties surrounding LG methane diffusive fluxes, it is difficult to accurately determine the overall contribution of methane to the atmosphere from the LG catchment and by extension from the GrIS margin as a whole.

To directly compare methane fluxes at the LG with those of other systems, we calculate the catchment-wide areal yield of $CH_{4(aq)}$ that contributed to the observed $CH_{4(aq)}$ lateral flux. When comparing catchment-area-normalized yields of $CH_{4(aq)}$, the lateral $CH_{4(aq)}$ flux from the LG translates into a yield higher than, or within the range of, other large rivers worldwide and highlights that the GrIS may act as a relatively important source of atmospheric methane (Extended Data Table 1; Supplementary Information 1c). Ultimately, the atmospheric footprint of GrIS CH_4 will partly depend on the overall surface area of the ice sheet that contributes to the overall diffusive fluxes, as well as on the magnitude of such fluxes at points of first contact between the atmosphere and subglacial runoff (for example, within open channels beneath the ice).

Stable-isotope analyses ($\delta^{13}C$ and $\delta^{2}H$) reveals that LG methane was microbial in origin, with most samples falling in a well defined range characteristic of acetoclastic methanogenesis, although with some degree of mixing with methane probably produced by a CO_2-reduction pathway (Fig. 4). This mixed origin of methane from CO_2 reduction and acetate fermentation is also supported by molecular evidence from the LG proglacial stream, which identifies the presence of 16S rRNA gene sequences related to both hydrogenotrophic and acetoclastic methanogens (Extended Data Fig. 4; Supplementary Information 2d). A mixed methane source at the LG suggests the availability of several methanogenic substrates beneath the ice, probably derived from the recycling of overridden old carbon (for example, acetate), such as that seen in GrIS marginal lakes[23], potentially supplemented by H_2 gas generated from rock comminution, which has been hypothesized to fuel methanogens beneath ice masses over extended glaciation[24] (see Supplementary Information 2d).

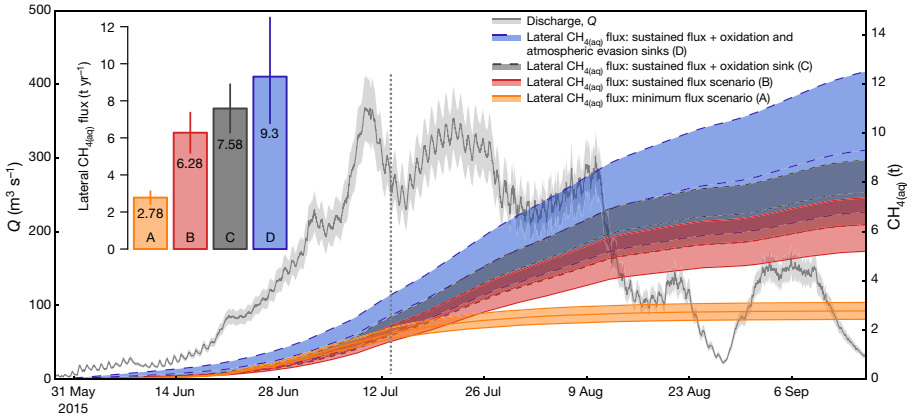

Fig. 2 | Cumulative lateral export of LG $CH_{4(aq)}$ over the 2015 melt season. Orange and red lines correspond to the minimum and sustained methane flux scenarios, respectively, at the measuring site (see Methods). Dark-grey lines represent a scenario that accounts for a methanotrophic methane sink on a sustained-flux scenario and represent the expected lateral methane flux that would have occurred without a methanotrophic sink. Blue lines correspond to a scenario that accounts for the combined estimated methanotrophic and diffusive flux sinks of methane before reaching the measuring site, added to a sustained-flux scenario. The vertical dotted line marks the last day of $CH_{4(aq)}$ sensor measurements (13 July). The width of the shaded areas corresponds to errors from sensor measurements and estimates of gas transfer velocities (see Methods). The pale-grey time series denotes discharge measurements over the entire melt season. The annual methane fluxes depicted in the bar plot correspond to the cumulative fluxes at the end of the melt season for each of the estimated scenarios; error bars correspond to the range depicted by the shaded areas.

Partial oxidation during transit from the subglacial system probably enriched the sampled methane with heavier stable isotopes[25] (Supplementary Information 2c), yet there is no strong isotopic trend that conclusively identifies methanotrophy as a major control on the isotopic signatures observed here (Fig. 4, Extended Data Fig. 3). This contrasts with patterns that we observed for stagnant waters beneath the LG proglacial river ice (Extended Data Fig. 3) and waters sampled from Antarctic Subglacial Lake Whillans (Supplementary Information 2c). We infer the limited methanotrophic signature observed here to reflect the largely anoxic conditions at the sites of methane production (and thus limited aerobic oxidation of methane) and the rapid evacuation of methane from the production site via a fast and efficient drainage system (Supplementary Information 2b).

The impact of subglacial methane on atmospheric concentrations partially depends on the presence of methane hydrates beneath ice sheets, as catastrophic methane hydrate destabilization during periods of rapid ice thinning could result in very large fluxes of methane to the atmosphere[3,4]. We used a one-dimensional reaction-transport model to identify the conditions required to allow methane hydrate formation beneath the LG catchment. Our results indicate that relatively high methanogenic rates (larger than those observed in Greenland basal ice incubation experiments[17]; Extended Data Fig. 5) and thick sediment layers (at least several tens of metres) are required to produce and sustain methane hydrates beneath the LG catchment (Supplementary Information 2e, f). The high methane flux that would be generated at the ice–sediment interface under methane hydrate conditions (estimated to be 10 to 1,000 times larger than the observed lateral flux, depending on hydrate conditions; Extended Data Fig. 6) makes it unlikely that a substantial portion (if any) of the exported CH_4 measured from the LG comes from subglacial methane hydrates. Importantly, however, the model results suggest that conditions favourable to hydrate formation are probably present in other regions of the GrIS with sustained thick ice cover (for example, for more than 10,000 years) and with thick sedimentary layers (for example, ref. [27]; Supplementary Information 2f).

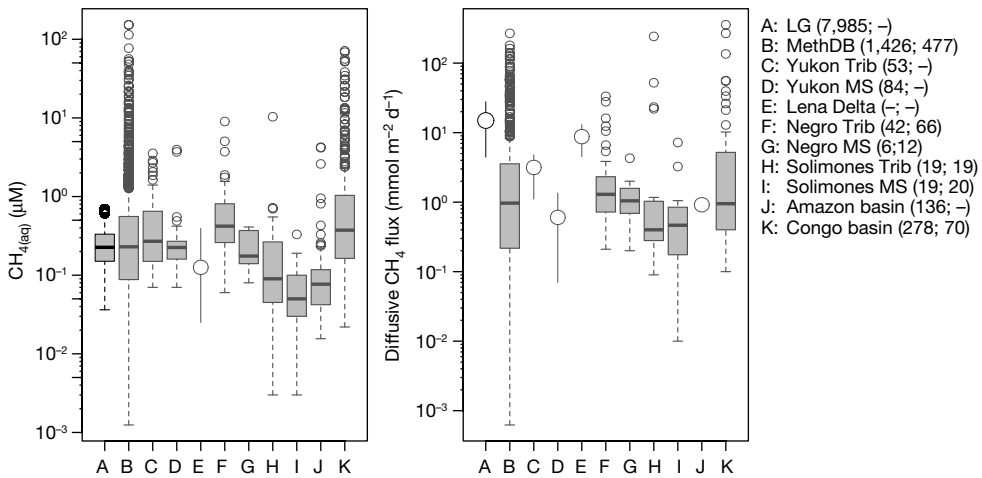

Fig. 3 | Box plots of $CH_{4(aq)}$ concentrations and diffusive fluxes for the LG and other major world river systems. The box mid-lines represent medians; the interquartile range (IQR) is represented by the lower and upper box boundaries, which denote the 25th and 75th percentiles, respectively; whiskers indicate confidence intervals 1.5 times the IQR, and points are outliers. The parentheses next to the names of the rivers give the number of observations for concentrations (left) and fluxes (right). Where no raw data are available, averages and reported ranges are depicted by circles and error bars (see Supplementary Information 1c for details). 'MethDB' refers to a worldwide $CH_{4(aq)}$ dataset for rivers[6]; 'Trib' and 'MS' refer to the tributaries and mainstems of the rivers, respectively.

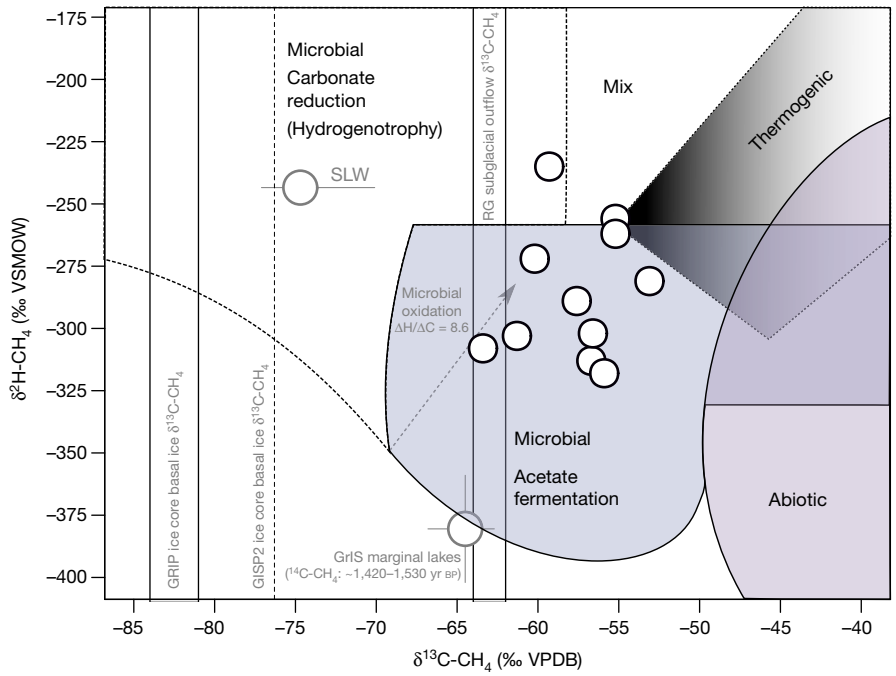

Fig. 4 | Carbon–hydrogen isotopic diagram of LG $CH_{4(aq)}$. Black-border points denote dual stable-isotope values ($\delta^{13}C$ and $\delta^{2}H$) for LG $CH_{4(aq)}$ samples (sample values are summarized in Extended Data Table 2). Average $\delta^{13}C$-CH_4 and $\delta^{2}H$-CH_4 values and ranges from Subglacial Lake Whillans (SLW) in Antarctica[3] and GrIS marginal lakes[24] are added as references (grey-border points), as well as $\delta^{13}C$-CH_4 data from GrIS ice-core basal ice[12,23] and from the subglacial outflows of the Greenland Russell Glacier (RG)[6] (marked by vertical lines). The estimated carbon age (years before present, BP) from ^{14}C analyses of methane from GrIS marginal lakes[24] is indicated next to point. The arrow denotes the microbial oxidation effect on CH_4 stable-isotope signatures; $\Delta H/\Delta C$ is the gradient (change in $\delta^{2}H$-CH_4 over change in $\delta^{13}C$-CH_4) of the arrow[26]. The classification zones and definitions of methane origins are derived and adapted from refs [25,26]. VSMOW, Vienna standard mean ocean water; VPDB, Vienna Pee Dee belemnite.

Using high-resolution in situ sensor measurements, we show that an extensive area of the GrIS continuously releases methane-supersaturated runoff from its bed during the melt season. Our results constitute the first measurements of sustained methane export from an ice-sheet catchment and highlight the need to better gauge the footprint of ice sheets on current methane budgets. The release of several tonnes of microbial methane from beneath the GrIS represents one of the strongest lines of evidence to date for considerable microbial production of methane in subglacial ecosystems and reinforces the view that large methane reserves may accumulate beneath past and present-day ice sheets[3,7]. This methane can reach the atmosphere where fast-flowing drainage networks enable its rapid transport beyond the ice margin before being oxidized to carbon dioxide, either driven by supraglacial forcing in the GrIS ablation zone or potentially also during episodic subglacial lake drainage events in Antarctica[28]. The influence of meltwater discharge on methane export observed here further suggests that projected increases in warming and melting rates could also lead to increases in subglacial methane release to the atmosphere. Our finding that subglacial environments in Greenland can generate high levels of methane emphasizes the need to directly measure methane reserves in subglacial systems containing high quantities of organic carbon, such as the thick sedimentary basins beneath the Antarctic Ice Sheet, where much larger amounts of methane, as hydrates, are expected to be present[4].

Online content

Any methods, additional references, Nature Research reporting summaries, source data, statements of data availability and associated accession codes are available at https://doi.org/10.1038/s41586-018-0800-0.

Received: 23 October 2017; Accepted: 8 November 2018;
Published online 2 January 2019.

1. Kirschke, S. et al. Three decades of global methane sources and sinks. *Nat. Geosci.* **6**, 813–823 (2013).
2. Schaefer, H. et al. A 21st century shift from fossil-fuel to biogenic methane emissions indicated by $^{13}CH_4$. *Science* **352**, 80–84 (2016).
3. Wadham, J. L., Tranter, M., Tulaczyk, S. & Sharp, M. Subglacial methanogenesis: a potential climatic amplifier? *Global Biogeochem. Cy.* **22**, GB2021 (2008).
4. Wadham, J. L. et al. Potential methane reservoirs beneath Antarctica. *Nature* **488**, 633–637 (2012).
5. Dieser, M. et al. Molecular and biogeochemical evidence for methane cycling beneath the western margin of the Greenland Ice Sheet. *ISME J.* **8**, 2305–2316 (2014).
6. Stanley, E. H. et al. The ecology of methane in streams and rivers: patterns, controls, and global significance. *Ecol. Monogr.* **86**, 146–171 (2016).
7. Weitemeyer, K. A. & Buffett, B. A. Accumulation and release of methane from clathrates below the Laurentide and Cordilleran ice sheets. *Global Planet. Change* **53**, 176–187 (2006).
8. Michaud, A. B. et al. Microbial oxidation as a methane sink beneath the West Antarctic Ice Sheet. *Nat. Geosci.* **10**, 582–586 (2017).
9. Petrenko, V. V. et al. Minimal geological methane emissions during the Younger Dryas–Preboreal abrupt warming event. *Nature* **548**, 443–446 (2017).
10. Portnov, A., Vadakkepuliyambatta, S., Mienert, J. & Hubbard, A. Ice-sheet-driven methane storage and release in the Arctic. *Nat. Commun.* **7**, (2016).
11. Souchez, R., Lemmens, M. & Chappellaz, J. Flow-induced mixing in the GRIP basal ice deduced from the CO_2 and CH_4 records. *Geophys. Res. Lett.* **22**, 41–44 (1995).
12. Miteva, V., Teacher, C., Sowers, T. & Brenchley, J. Comparison of the microbial diversity at different depths of the GISP2 Greenland ice core in relationship to deposition climates. *Environ. Microbiol.* **11**, 640–656 (2009).
13. Christner, B. C., Montross, G. G. & Priscu, J. C. Dissolved gases in frozen basal water from the NGRIP borehole: implications for biogeochemical processes beneath the Greenland Ice Sheet. *Polar Biol.* **35**, 1735–1741 (2012).
14. Schmidt, M., Linke, P. & Esser, D. Recent development in IR sensor technology for monitoring subsea methane discharge. *Mar. Technol. Soc. J.* **47**, 27–36 (2013).
15. Cowton, T., Nienow, P., Bartholomew, I., Sole, A. & Mair, D. Rapid erosion beneath the Greenland ice sheet. *Geology* **40**, 343–346 (2012).
16. Kohler, T. J. et al. Carbon dating reveals a seasonal progression in the source of particulate organic carbon exported from the Greenland Ice Sheet. *Geophys. Res. Lett.* **44**, 6209–6217 (2017).
17. Stibal, M. et al. Methanogenic potential of Arctic and Antarctic subglacial environments with contrasting organic carbon sources. *Glob. Change Biol.* **18**, 3332–3345 (2012).
18. Bartholomew, I. et al. Supraglacial forcing of subglacial drainage in the ablation zone of the Greenland ice sheet. *Geophys. Res. Lett.* **38**, L08502 (2011).
19. Raymond, P. A. et al. Global carbon dioxide emissions from inland waters. *Nature* **503**, 355–359 (2013); erratum **507**, 387 (2013).

20. Chandler, D. M. et al. Evolution of the subglacial drainage system beneath the Greenland Ice Sheet revealed by tracers. *Nat. Geosci.* **6**, 195–198 (2013).
21. Hall, R. O., Kennedy, T. A. & Rosi-Marshall, E. J. Air–water oxygen exchange in a large whitewater river. *Limnol. Oceanogr. Fluids Environ.* **2**, 1–11 (2012).
22. Maurice, L., Rawlins, B. G., Farr, G., Bell, R. & Gooddy, D. C. The influence of flow and bed slope on gas transfer in steep streams and their implications for evasion of CO_2. *J. Geophys. Res. Biogeosci.* **122**, 2862–2875 (2017).
23. Walter Anthony, K. M., Anthony, P., Grosse, G. & Chanton, J. Geologic methane seeps along boundaries of Arctic permafrost thaw and melting glaciers. *Nat. Geosci.* **5**, 419–426 (2012).
24. Telling, J. et al. Rock comminution as a source of hydrogen for subglacial ecosystems. *Nat. Geosci.* **8**, 851–855 (2015); erratum 8, 981 (2015).
25. Whiticar, M. J. Carbon and hydrogen isotope systematics of bacterial formation and oxidation of methane. *Chem. Geol.* **161**, 291–314 (1999).
26. Etiope, G. & Sherwood Lollar, B. Abiotic methane on Earth. *Rev. Geophys.* **51**, 276–299 (2013).
27. Walter, F., Chaput, J. & Lüthi, M. P. Thick sediments beneath Greenland's ablation zone and their potential role in future ice sheet dynamics. *Geology* **42**, 487–490 (2014).
28. Wingham, D. J., Siegert, M. J., Shepherd, A. & Muir, A. S. Rapid discharge connects Antarctic subglacial lakes. *Nature* **440**, 1033–1036 (2006).

Acknowledgements We thank all of those who assisted with fieldwork at LG, especially J. Hatton, as well as F. Sgouridis and J. Williams at the LOWTEX laboratory of the University of Bristol. This research is part of the UK NERC-funded DELVE programme (NERC grant NE/I008845/1 to J.L.W.). G.L.-G. was funded by the University of Bristol Scholarship Programme and a FRQNT Scholarship (number 185136). The work was also supported by a Leverhulme research fellowship to J.L.W., a UK NERC grant (NE/J02399X/1) to A.M.A. for DNA analyses, as well as Czech Science Foundation grants (GACR; 15-17346Y and 18-12630S) to M.S. Isotopic analyses were conducted by G. Lacrampe-Couloume at the University of Toronto with support provided by the Natural Sciences and Engineering Research Council of Canada (NSERC) to B.S.L. We also thank the Kangerlussuaq International Science Station, especially R. Møller, for support with field logistics, as well as M. A. Cooper, M. Macdonald and S. Hoffer for comments.

Reviewer information *Nature* thanks J. Crawford and the other anonymous reviewer(s) for their contribution to the peer review of this work.

Author contributions J.L.W. and G.L.-G. designed the study. B.S.L. supervised the stable-isotope analyses. S.A. performed the reaction-transport hydrate model calculations. P.F. assisted in the interpretation and analysis of the CONTROS HydroC CH_4 raw results. G.L.-G., J.T., E.A.B., A.D.B., M.C.M. and J.R.H. conducted field logistical preparations. J.L.W., J.T. and M.S. led the 2015 Greenland field campaign. G.L.-G., A.D.B., A.J.T., J.T., E.A.B., J.R.H., T.J.K., J.D.Z. and M.S. collected the sensor field data. G.L.-G. and J.D.Z. collected manual water samples in the field. G.L.-G. and A.M.A. analysed molecular data. G.L.-G. performed the data analysis and wrote the manuscript with significant contribution from all co-authors.

Competing interests P.F. works for the sensor manufacturer Kongsberg Maritime Contros, but the sensor data discussed here were validated by independent measurements. The other authors declare no competing interests.

Additional information
Extended data is available for this paper at https://doi.org/10.1038/s41586-018-0800-0.
Supplementary information is available for this paper at https://doi.org/10.1038/s41586-018-0800-0.
Reprints and permissions information is available at http://www.nature.com/reprints.
Correspondence and requests for materials should be addressed to G.L.
Publisher's note: Springer Nature remains neutral with regard to jurisdictional claims in published maps and institutional affiliations.

METHODS

Site description and hydrogeochemical analyses. The hydrology of the LG has been extensively studied and described previously (see Supplementary Information 1a). A detailed description of the proglacial study site, as well as the hydrological and geochemical monitoring performed during the 2015 melt season, can be found in two parallel studies[16,29]. In brief, a suite of hydrogeochemical sensors recording pH (Honeywell Durafet), water temperature (Aanderaa and Campbell Scientific), electrical conductivity (Campbell Scientific 547) and turbidity (Partech C) were deployed in the LG proglacial river, about 1.6 km downstream from the subglacial ice portal at the glacier's terminus (Extended Data Fig. 1). Turbidity measurements were converted to suspended sediment concentrations by calibration against manual sediment samples collected over the span of the melting season, as in ref. [30]. Discharge measurements were derived from pressure transducers (Druck and Hobo) and stage sensors (Campbell Scientific SR50A) fixed in a bedrock section about 2 km downstream from the glacier's terminus. Stage measurements were converted to discharge values using a stage–discharge rating curve generated from calibration against repeated rhodamine dye injections over the full range of river stages during the melt season, as in ref. [18]. Uncertainties (root-mean-square deviation) on discharge measurements were calculated to be about 12.1%.

Manual sampling. Manual samples were collected a few metres (about 5–10 m) upstream of the HydroC sensor. Water samples were collected inside pre-evacuated (at most 500 mTorr) 120-ml borosilicate vials sealed with 2-cm-thick butyl-rubber stoppers, pre-flushed with 5.0 grade argon and pre-poisoned with about 24 mg of $HgCl_2$ to fix the samples and prevent any microbial activity from affecting the gases post-sampling, after the method of ref. [31]. 10 ml (at room temperature and pressure) of helium (grade 5.0) was added to the evacuated vials to maintain a headspace during sampling. Most water samples ($n = 53$) were collected using a peristaltic pump (Portapump-810, Williamson Manufacturing) equipped with silicone tubing; a small number of samples were collected using plastic syringes ($n = 2$) or passively, using the vials' vacuum pressure by directly piercing the septum of submerged vials with a needle ($n = 8$). Vials containing apparent air contamination or vacuum loss (for example, resulting in abnormally large headspace post-sampling) were excluded from analyses. Samples for stable-isotope analysis were collected as above ($n = 9$ collected using the peristaltic pump, $n = 2$ using syringes).

Methane concentrations were calculated using the headspace method. Headspace samples were analysed on an Agilent 7980A gas chromatograph equipped with a Porapak Q 80–100 mesh, 2.5 m × 2.0 mm stainless-steel column and flame-ionization detector. Standard curves were calculated from certified (±5%) gas-standard measurements. Gas concentrations were converted to molar concentrations using the ideal gas law, and dissolved methane concentrations were obtained using Bunsen coefficients[32]. Internal vial pressures were calculated using the ideal gas law from the difference between the headspace volume post-sampling and the theoretical headspace volume of 10 ml at 1 atm and 20 °C. An average internal pressure of 3.5 ± 0.9 atm (standard deviation) was assigned to all manual samples for calculations.

CONTROS HydroC CH_4 sensor. Methane measurements were performed using a CONTROS HydroC CH_4 system (Kongsberg Maritime), an optical (infrared), headspace-based underwater sensor. An underwater pump (SBE 5T, Sea-Bird Scientific) mounted to the sensor continuously feeds water to the membrane equilibrator. Dissolved gases diffuse through a composite membrane into the internal gas circuit, where partial pressure is measured using tunable diode laser absorption technology[14]. The CONTROS HydroC sensor was deployed completely submerged, within a solid metallic cage moored by cables attached to boulders on the river bank, with the sensor head facing the river current (Extended Data Fig. 1). Measurements were logged every minute between 19 May and 4 June; the logging interval was changed to 5 min on 4 June until the end of the measuring period, on 13 July.

The ideal gas law and Bunsen coefficients were used to convert microatmosphere-scale measurements (Extended Data Fig. 7c) to molar concentrations (Fig. 1). Water temperatures (±0.05 °C reported accuracy) were recorded using an Aanderaa Optode 3830 sensor deployed in parallel (Extended Data Fig. 7a). The reported overall uncertainty of CONTROS HydroC CH_4 is 2 μatm (about 5 nM) or ±3% of the reading, whichever is greater.

Calculation of lateral methane flux. The $CH_{4(aq)}$ measurements stopped on 13 July. $CH_{4(aq)}$ fluxes estimated during the rest of the ablation season were based on two scenarios: (i) assuming that methane levels would immediately decrease until they reached river baseline concentrations on 15 September (last discharge measurement), or (ii) assuming that methane levels would continue to follow a discharge-dependent trend for the duration of the ablation season.

(i) Constant concentration decrease (annual lateral CH_4 flux of 2.78 t). In the constant-concentration-decrease scenario, a baseline $CH_{4(aq)}$ concentration was set on the basis of manual water samples collected during a return visit to the sampling site on 28 October, when the proglacial river was partially frozen and no runoff contribution to the proglacial river stream was apparent. The October concentrations averaged about 18.5 nM (beneath river ice at that time; $n = 6$).

The minimum flux scenario was calculated using a natural-logarithm decrease of the form

$$y = Ce^{-kt}$$

where y is the methane flux (for example, in grams per second), C is the last flux measurement, obtained on 13 July (that is, 0.71 g s^{-1}), t is the time elapsed between 13 July and the measurement of flux y, and k is the reaction constant, obtained assuming a baseline concentration of 18.5 nM and using a discharge of 32 m^3 s^{-1} (last discharge measurement, on 15 September).

(ii) Sustained flux (annual lateral CH_4 flux of 6.28 t). The sustained-flux scenario was calculated using the discharge-weighted mean $CH_{4(aq)}$ concentration of 271 ± 34 nM, obtained from measurements up to 13 July; the error reflects errors on discharge measurements (12.1%) as well as measurement errors of the HydroC CH_4 sensor (2 μatm or 3%, whichever is greater).

Estimation of methane sink via methanotrophic oxidation. The methane concentrations recorded at the LG probably underestimate the original methane levels present beneath the catchment because of the water travel time between the subglacial methane source and the measurement site. In addition to atmospheric evasion of methane, aerobic microbial oxidation of methane would have lowered methane concentrations before reaching the observation site, once fully oxygenated meltwater runoff entered the subglacial system (O_2 concentrations in runoff were either near atmospheric equilibrium or supersaturated for most of the monitoring period; Extended Data Fig. 7a). Methanotrophy was observed qualitatively in a small number of unfixed river samples collected in parallel with fixed manual samples. Analyses at the home laboratory showed $CH_{4(aq)}$ concentrations decreased by a factor of up to 100 in unfixed samples compared with the fixed vials (data not shown). However, no time series incubation was set up and consequently no methanogenic rates were calculated for the LG site.

The quantity of methane oxidized by methanotrophic bacteria before reaching the measuring site was estimated using the methanotrophic rate reported for the marginal stream of the neighbouring Russell Glacier (that is, 0.32 μM d^{-1})[5]. Justifications for using the Russell Glacier oxidation rate are discussed in Supplementary Information 2c. The time during which runoff was subject to methane oxidation (that is, water travel time) was estimated from water velocities and subglacial drainage evolution calculated on the basis of a previous study at the LG[20]. We assumed that subglacial aerobic methane oxidation occurs between the location of supraglacial runoff–input, where oxygenated supraglacial waters enter the subglacial system, and the measuring site located 1.6 km downstream of the LG glacier terminus.

Water velocities were calculated using the relationship between maximum tracer velocity (v_{05}) and cumulative discharge ($\sum Q$), described for the gaseous tracer SF_6 in ref. [20], which takes the form

$$v_{05} = A \ln(\Sigma Q) + B$$

with the regression parameters A and B calculated to be 0.235 m s^{-1} and −3.59 m s^{-1}, respectively[20]. We fixed the minimum velocity at 0.4 m s^{-1}, which corresponds to the minimum v_{05} calculated in ref. [20] for tracer injections performed 7 km inland from the LG portal at times of low cumulative discharge.

We estimated the inland evolution of an efficient channelized subglacial hydrological system on the basis of the relationship between cumulative discharge and v_{05} at moulin injection sites (see figure 2a in ref. [20]). We derived the progression of supraglacial water inputs using the lowest value of cumulative discharge, observed where v_{05} at an injection site fell onto the regression line of v_{05} on the cumulative discharge for the L7 injection in ref. [20] (see supplementary figure 2.8 in ref. [20]). That is, we assumed that the channelized subglacial channel would reach 7 km at a cumulative discharge of 1.9×10^7 m^3, 14 km at 9.4×10^7 m^3 and 41 km at 7.8×10^8 m^3 on the basis of supplementary figure 2.8 and supplementary table 1 in ref. [20]. Although we acknowledge that such calculations are approximate at best, they allow the use of a dynamic distance of travel during the melt season. We fixed the maximum travel distance at 41 km from the LG terminus, after which the LG subglacial system is considered to become primarily inefficient and distributed for the duration of the ablation season[20]. To account for potential methane sources and methanotrophic activity occurring downstream of the supraglacial-runoff input into the subglacial channelized system, we used an average distance of travel in our calculation (that is, half of the distance of travel obtained from the cumulative-discharge calculations above).

Calculation of diffusive methane flux. Accurately calculating methane losses due to atmospheric evasion was beyond the scope of the present study, and therefore flux numbers should be considered conservative estimates of the amount of methane originally generated and exported from the LG catchment.

Diffusive fluxes for the LG stream were estimated following the approach in ref. [19], which estimates gas transfer velocity coefficients (k) from the stream slope and water velocity (fitted equation (5) in ref. [33]). Fluxes were estimated for the first 1.6 km of the proglacial river, from the ice margin to the measuring site. The stream slope was obtained from Google Earth and approximated as 0.04; slope values of 0.01, 0.03 and 0.05 were used to generate minimum, medium and maximum k values, respectively. A water velocity of 1 m s^{-1} was used, which corresponds to the discharge weighted mean of subglacial water velocities (v_{05}) used for methanotrophic sink calculations (see above).

Methane gas-transfer velocities (k_{CH4}) were converted from the calculated k_{600} values following relationships between Schmidt numbers and k for CO_2 and CH_4 (see equations (2) and (3) in ref. [33]); Schmidt numbers were calculated using an average water temperature of 0.22 °C (Extended Data Fig. 7d)[34]. Minimum, medium and maximum slope values, as well as standard deviations on k_{600} equation parameters[33], resulted in minimum, medium and maximum k_{CH4} of 16 m d^{-1}, 49 m d^{-1} and 84 m d^{-1}, respectively.

Methane diffusive fluxes were calculated using the discharge-weighted mean $CH_{4(aq)}$ concentration for the observation period (271 nM) and assuming an atmospheric methane concentration of 1.8 p.p.m. by volume (resulting in an equilibrium concentration of about 4.6 nM). Diffusive flux upstream of the measuring site was calculated using 1-m retroactive bins, adjusting upstream dissolved methane concentrations for methane loss by both diffusive flux and microbial oxidation losses in downstream bins; a fixed river width of 40 m, water velocity of 1 m s^{-1} and average discharge of 150 m^3 s^{-1} were used in the calculations. The reported diffusive flux values correspond to the average flux calculated for the 1.6 km of stream for each minimum, medium and maximum scenarios. Cumulative fluxes were calculated for the discharge measurement period (that is, about 110.5 days) and normalized to estimated water velocities (see previous section). Details on the diffusive fluxes of other world rivers can be found in Supplementary Information 1c.

Stable-isotope analyses. Analyses for $\delta^{13}C$ values were performed by continuous-flow compound-specific carbon-isotope-ratio mass spectrometry with a Finnigan MAT 252 mass spectrometer interfaced with a Varian 3400 capillary gas chromatograph. Hydrocarbons were separated by a Poraplot Q column (25 m × 0.32 mm internal diameter) with the following temperature programme: initial temperature 40 °C, hold for 1 min, increase to 190 °C at 5 °C min^{-1}, hold for 5 min. The total error, incorporating both accuracy and reproducibility, is ±0.5‰ with respect to the Vienna Pee Dee belemnite standard[35]. The δ^2H analysis was performed on a continuous-flow compound-specific hydrogen-isotope mass spectrometer that consists of an HP 6890 gas chromatograph interfaced with a micropyrolysis furnace (1,465 °C) in line with a Finnigan MAT Delta$^+$-XL isotope-ratio mass spectrometer. H_2 and CH_4 were separated by a molecular sieve 5A column (25 m × 0.32 mm internal diameter) with a carrier gas flow rate of 1.2 ml min^{-1} and the temperature programme: initial temperature 20 °C, hold for 5 min, followed by an increase to 280 °C at 25 °C min^{-1}. Higher hydrocarbons were separated using the same column and temperature programme as those used in the carbon isotope analysis. The total error, incorporating both accuracy and reproducibility, for the hydrogen isotope analysis is ±5‰ with respect to V-SMOW[31].

Methane hydrates. To evaluate the potential for hydrate formation beneath the LG catchment, we used a one-dimensional reaction-transport model that was originally developed for simulating hydrate formation in marine sediments[36] and has previously been adapted for subglacial Antarctica[4]. We assumed physical properties for sediments similar to those previously used for ocean sediment modelling[36]. Extended Data Table 3 summarizes site-specific model parameters, their model values and units. The model solves the one-dimensional diffusion–advection–reaction equations for dissolved methane, gaseous methane and methane hydrates. The implemented reaction network accounts for a constant methane production rate R_{xn} over a predefined sediment depth z_{xn}, methane hydrate, as well as methane gas formation and dissociation. At the upper boundary, the boundary concentrations were set to zero (that is, Dirichlet boundary condition), reflecting warm-based conditions and allowing for diffusive flux of methane through the ice-sediment interface. In addition, the initial conditions for dissolved and gaseous methane and methane hydrates were set to zero. A 'best case' scenario was designed to reflect optimal, but plausible, physical and biogeochemical conditions for hydrate formation to assess the maximum potential for hydrate accumulation in the catchment. More specifically, we assigned a thick methanogenic sediment layer beneath the catchment (that is, up to 100 m), a 10,000-year ice-sheet overburden to allow for hydrate evolution, complete anoxic conditions, an overlaying ice thickness set to 1,000 m (ice thickness over the LG catchment exceeds 1,000 m at about 39 km from the ice margin[20]), a basal temperature of −1 °C, and absence of a methane sink within the sediment layer (for example, no anaerobic oxidation of methane). This 'best case' model setup was run over a wide range of constant methane production rates (R_{xn} of 10^{-17} to 10^{-13} grams CH_4 per gram of wet sediment per second) to determine the order of magnitude of methane production rates required to accumulate hydrates. After this initial screening, methane production rates were varied systematically between 10^{-15} to 10^{-14} grams CH_4 per gram of wet sediment per second.

Data availability

The data used in this article are available from the corresponding author on request. The 16S rRNA gene sequence data are available from the NCBI Sequence Read Archive (https://www.ncbi.nlm.nih.gov/sra) under BioProject PRJNA495593 (BioSamples SAMN10228172-SAMN10228185; SAMN10228190-SAMN10228206).

29. Beaton, A. D. et al. High-resolution in situ measurement of nitrate in runoff from the Greenland Ice Sheet. *Environ. Sci. Technol.* **51**, 12518–12527 (2017).
30. Hawkings, J. R. et al. Ice sheets as a significant source of highly reactive nanoparticulate iron to the oceans. *Nat. Commun.* **5**, 3929 (2014).
31. Ward, J. A. et al. Microbial hydrocarbon gases in the Witwatersrand Basin, South Africa: implications for the deep biosphere. *Geochim. Cosmochim. Acta* **68**, 3239–3250 (2004).
32. Wiesenburg, D. A. & Guinasso, N. L., Jr. Equilibrium solubilities of methane, carbon monoxide, and hydrogen in water and sea water. *J. Chem. Eng. Data* **24**, 356–360 (1979).
33. Raymond, P. A. et al. Scaling the gas transfer velocity and hydraulic geometry in streams and small rivers. *Limnol. Oceanogr. Fluids Environ.* **2**, 41–53 (2012).
34. Wanninkhof, R. Relationship between wind speed and gas exchange over the ocean revisited. *Limnol. Oceanogr. Methods* **12**, 351–362 (2014).
35. Sherwood Lollar, B., Hirschorn, S. K., Chartrand, M. M. G. & Lacrampe-Couloume, G. An approach for assessing total instrumental uncertainty in compound-specific carbon isotope analysis: implications for environmental remediation studies. *Anal. Chem.* **79**, 3469–3475 (2007).
36. Davie, M. K. & Buffett, B. A. A numerical model for the formation of gas hydrate below the seafloor. *J. Geophys. Res.* **106**, 497–514 (2001).
37. Tedesco, M. et al. Evidence and analysis of 2012 Greenland records from spaceborne observations, a regional climate model and reanalysis data. *Cryosphere* **7**, 615–630 (2013).
38. Palmer, S., Shepherd, A., Nienow, P. & Joughin, I. Seasonal speedup of the Greenland Ice Sheet linked to routing of surface water. *Earth Planet. Sci. Lett.* **302**, 423–428 (2011).

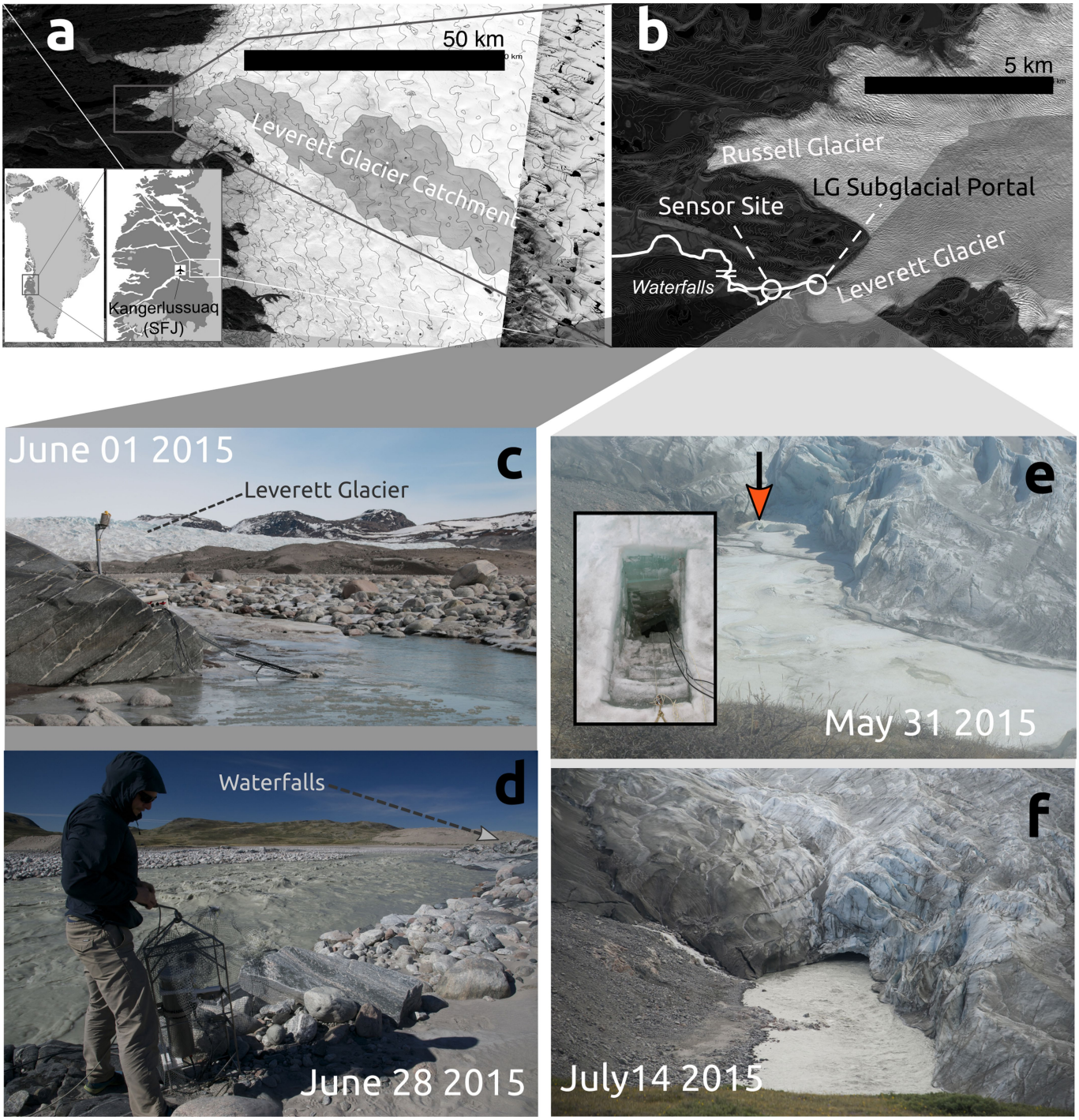

Extended Data Fig. 1 | Leverett Glacier and proglacial stream. **a**, Leverett Glacier (LG), with catchment boundaries[38] outlined in grey; 'SFJ' denotes the Kangerlussuaq airport. **b**, Zoomed image of the LG, with the sampling site and portal marked by dots. **c**, Sensor deployment site during the early melt season, with the LG visible in the background; the image faces upstream. **d**, Sensor deployment site in late June; the image faces downstream. Also visible is the HydroC sensor inside a steel cage, during inspection and before redeployment. **e**, LG portal in late May, while still covered with both glacial and river ice. The photograph was taken one hour before the appearance of the glacial upwelling (see Supplementary Information 2b). The arrow marks the location of the chainsawed hole, shown in the inset (photograph taken on 10 May 2015). **f**, LG portal in mid-July 2015. Map images from USGS/NASA Landsat.

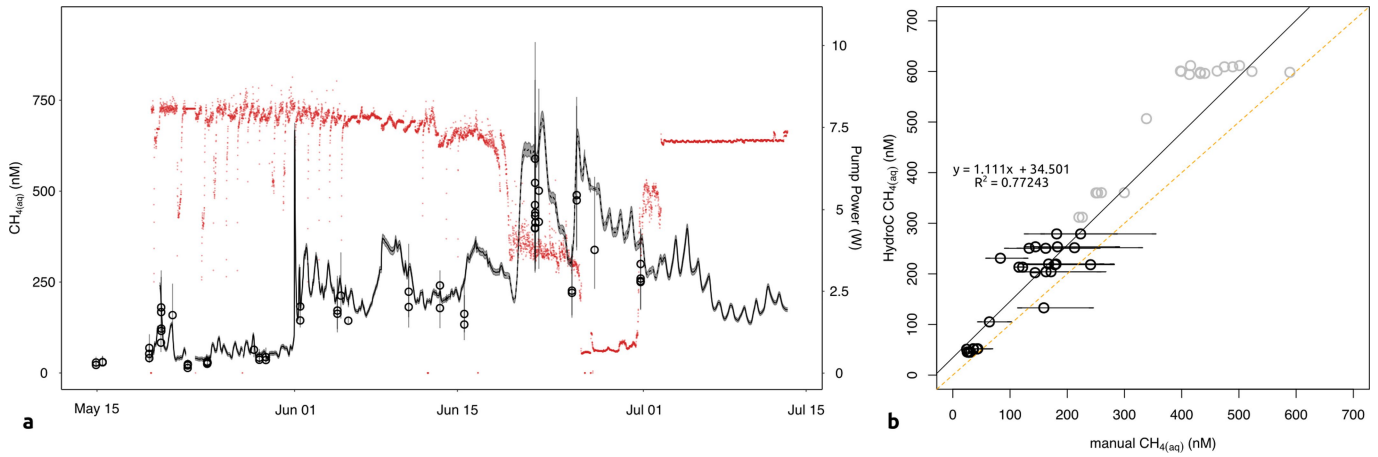

Extended Data Fig. 2 | Comparison of $CH_{4(aq)}$ concentrations measured with the HydroC sensor and from manual samples. a, $CH_{4(aq)}$ time series. Red points correspond to the HydroC pump power during operation. The continuous line depicts HydroC measurements, with the dashed section corresponding to times when the sensor experienced low pump power and thus a reduced water flow induced by the pump (19 June to 1 July). Open circles correspond to manual samples. The thin grey-shaded area around the $CH_{4(aq)}$ time series corresponds to the uncertainty of the HydroC measurements (about 3%). The uncertainty on manual measurements, indicated by the error bars, reflects the error on vial internal pressures and volumes (119 ± 0.76 ml, where the uncertainty represents standard deviation; internal pressures are derived from volumes—see Methods for details). **b**, Regression plot between the HydroC and manual sample measurements. Only manual samples taken during times when the HydroC pump power was above about 7 W were considered for the regression (black circles, black line); grey circles correspond to samples taken during times of lower pump power. Horizontal error bars reflect errors on manual measurements; vertical error bars are smaller than the size of the markers. The orange dashed line depicts a hypothetical 1:1 relationship between the sensor and manual measurements.

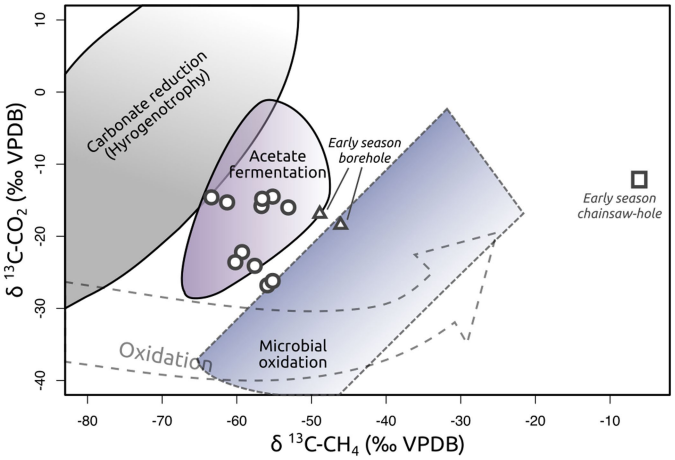

Extended Data Fig. 3 | Combination plot of $\delta^{13}C\text{-}CO_2$ and $\delta^{13}C\text{-}CH_4$ of LG runoff. Points denote $\delta^{13}C$ CO_2-CH_4 values for LG manual samples. Methanogenesis and microbial oxidation classification zones are derived and adapted from ref. [25].

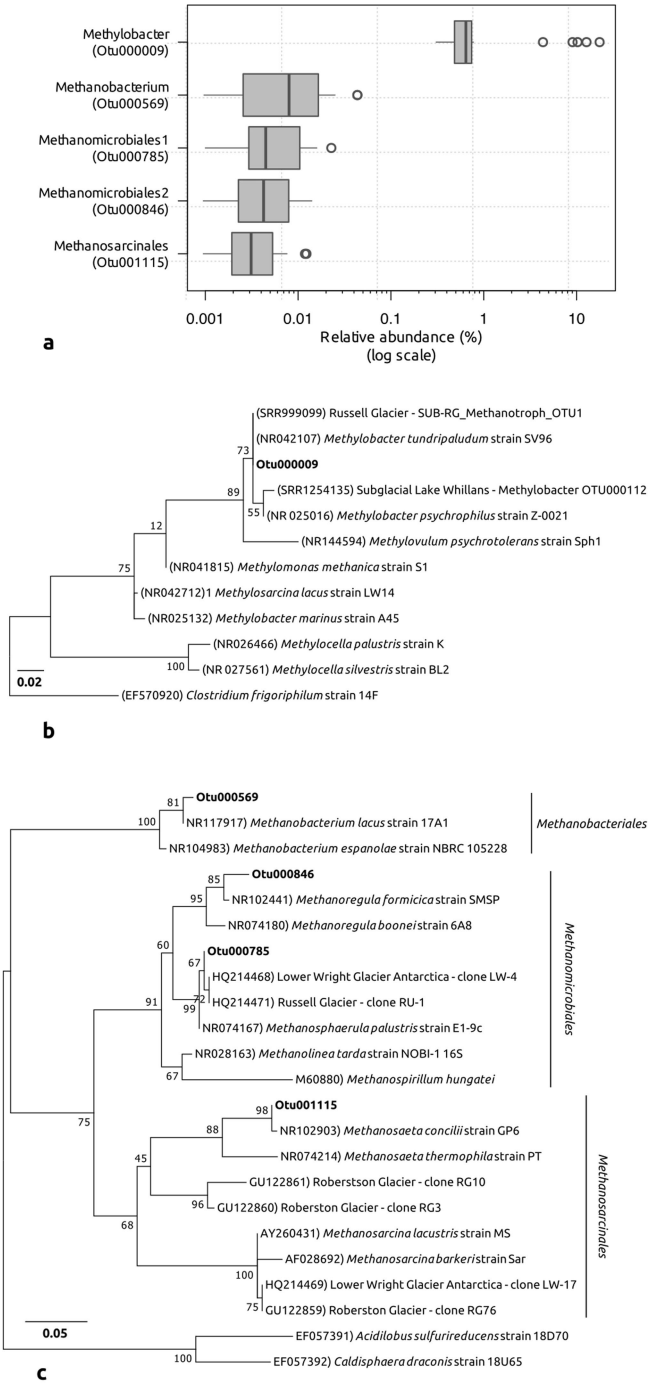

Extended Data Fig. 4 | LG 16S rRNA gene sequences related to methanotrophic and methanogenic clades. a, Relative abundance of the dominant operational taxonomical units related to bacterial methanotrophs (OTU00009) and archaeal methanogens. The box mid-lines represent medians; the IQR is represented by the lower and upper box boundaries and denote the 25th and 75th percentiles, respectively; whiskers indicate confidence intervals of 1.5 times the IQR, and points are outliers. **b**, **c**, Maximum-likelihood trees of 16S rRNA sequences related to methanotrophs rooted with the sequences of *Clostridium frigoriphilum* (**b**) and methanogens rooted with the sequences of *Acidibilus sulfurireducens* and *Caldisphaera draconis* (**c**).

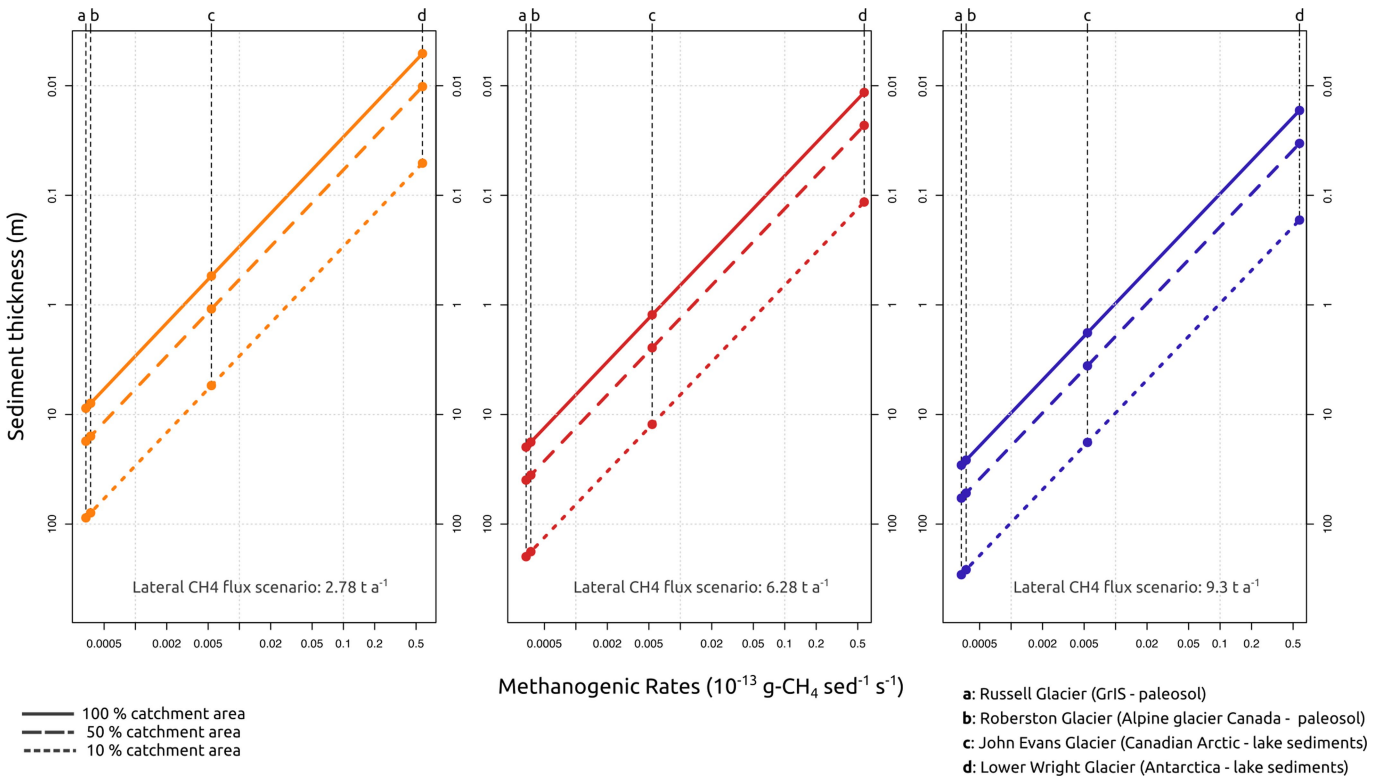

Extended Data Fig. 5 | Relationship between rates of subglacial methanogenesis, sediment thickness and observed annual CH_4 flux at LG. Each panel corresponds to the different yearly lateral $CH_{4(aq)}$ flux estimates measured in 2015 (see Fig. 2). Each line type corresponds to the sediment thickness required under different catchment area conditions: 100% (solid line), 50% (long-dashed line) or 10% (short-dashed line) of the subglacial catchment to contribute to the observed CH_4 flux. Any point on a line corresponds to the methanogenesis rate and subglacial sediment thickness required to generate the observed lateral CH_4 flux. The four points on each line correspond to known methanogenic rates recorded from different subglacial habitats[17].

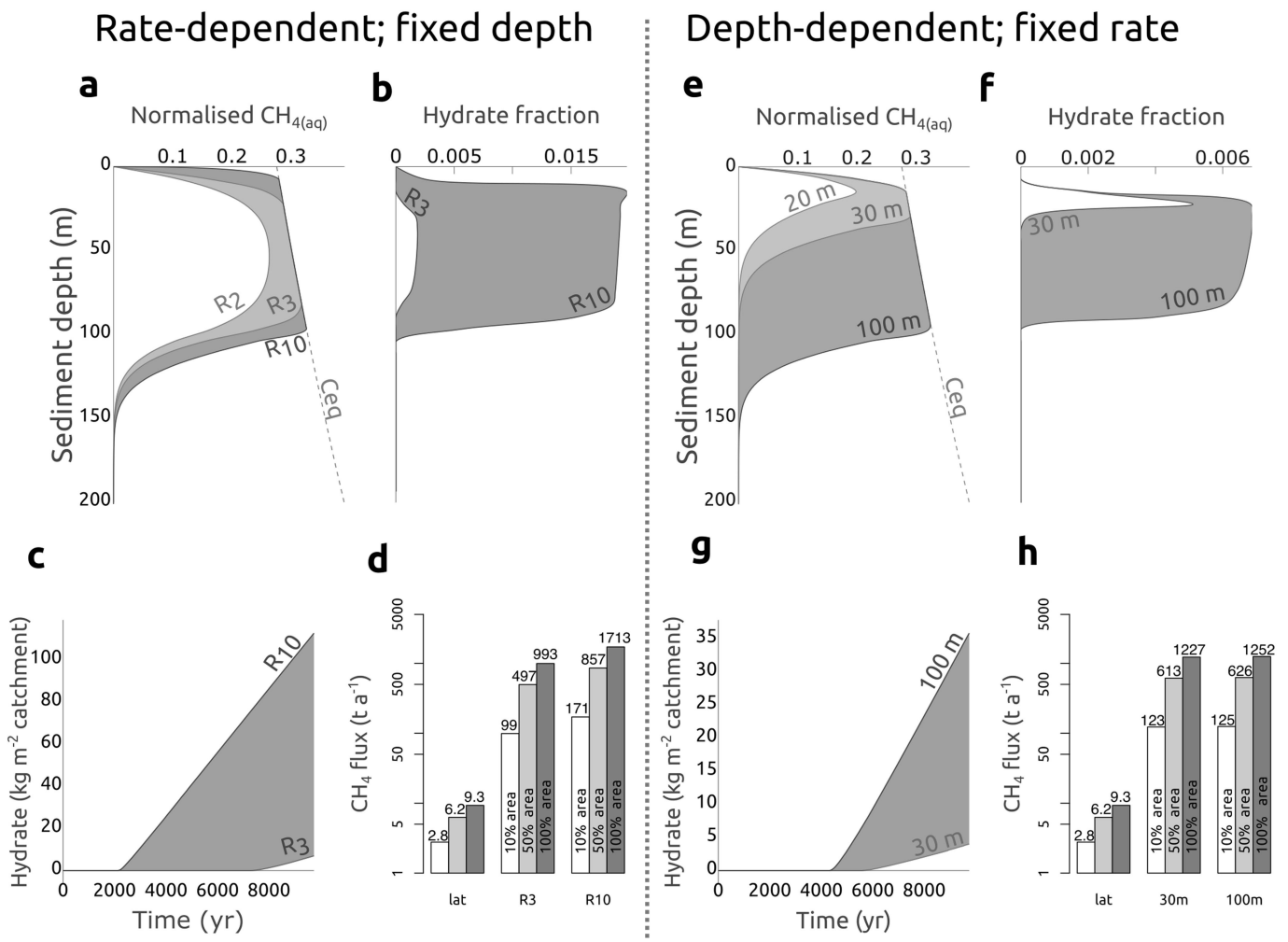

Extended Data Fig. 6 | Summary of model conditions required for subglacial methane hydrate formation. a–d, Model results for a fixed methanogenic depth (100 m) but varying methanogenic rates (R_2 to R_{10}; that is, 2×10^{-15} to 10×10^{-15} grams CH_4 per gram of sediment per second). **e–h**, Outputs of model runs under a fixed methanogenic rate (5×10^{-15} grams CH_4 per gram of sediment per second) but varying methanogenic depths (20–100 m). **a**, **b**, **e**, **f**, Vertical profiles of methane solubility, dissolved methane and methane hydrates; methane concentrations are normalized to equilibrium concentration. **c**, **g**, Time required for methane hydrate formation under the modelled conditions. **d**, **h**, Diffusive CH_4 flux at the sediment–ice interface under methane hydrate conditions assuming three different catchment cover areas for methane hydrates (that is, 10%, 50% and 100% of the LG catchment), compared to the three lateral flux scenarios (**a**, **b**, **d**; Fig. 2); see Supplementary Information 2f.

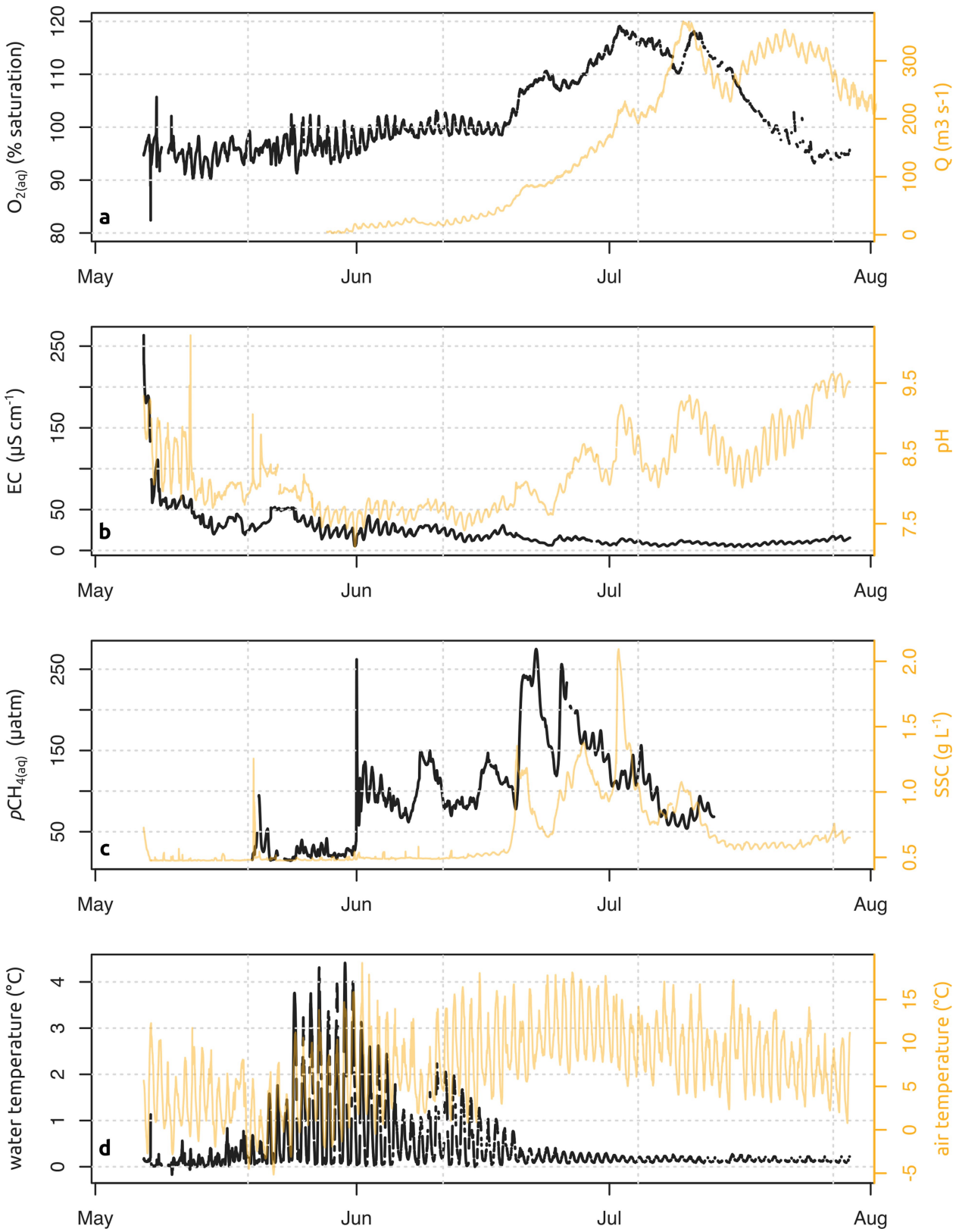

Extended Data Fig. 7 | Extended time series of geochemical measurements from the LG proglacial river. a–d, The EC, pH and SSC time series include those depicted in Fig. 1 but extend to measurements before and after the methane record. It should be noted that the $CH_{4(aq)}$ data in **c** are the HydroC partial pressure (in microatmospheres) measurements. Left and right vertical axes correspond to black and orange datasets, respectively.

Extended Data Table 1 | $CH_{4(aq)}$ concentration, fluxes and areal yield from LG, the GrIS and other world rivers

River	Catchment Area (10^6 km^2)	Discharge (km^3 a^{-1})	Concentration (μM $CH_{4(aq)}$)	Diffusive flux (mmol-CH_4 m^{-2} d^{-1})	Diffusive flux (Gg-CH_4 a^{-1})	Lateral flux (Gg-$CH_{4(aq)}$ a^{-1})	Areal Yield Diffusive (mmol-CH_4 m^{-2} a^{-1})	Areal Yield Lateral (mmol-$CH_{4(aq)}$ m^{-2} a^{-1})
LG runoff	**0.0006**	**1.45**	**0.27**	**14.94**	**-**	**0.0063**	**-**	**0.65**
GrIS runoffs†	-	*418* ‡	*0.27*	-	-	*2.1*	-	-
Lena Delta	2.49	821	0.07	9.22	150	0.9	3.8	0.02
Yukon Trib	0.19	48	0.75	3.16	12	0.6	4.0	0.19
Yukon MS	0.82	206	0.38	0.60	8	1.3	0.6	0.10
Negro Trib	0.69	455	0.87	-	-	6.0	-	1.29
Negro MS	0.69	1634	0.26	2.00	79	4.2	7.2	0.38
Solimões Trib	0.99	1985	0.33	-	-	10.6	-	1.17
Solimões MS	0.99	3507	0.06	1.60	160	3.3	10.1	0.21
Amazon	6.03	5444	0.18	0.92	490	15.5	5.1	0.16
Congo	3.71	1270	3.17	16.42	1906	64.6	32.1	1.10

Diffusive fluxes are calculated as grand means, except for the LG runoff diffusive flux, which corresponds to the medium flux scenario (scenario B in Fig. 2; see Methods for details). Except for the Amazon and Congo, lateral fluxes and yields are calculated using discharge-weighted means; see Supplementary Information 1c for references and calculation details.
†The GrIS-wide $CH_{4(aq)}$ flux was estimated using the LG discharge-weighted $CH_{4(aq)}$ concentration mean applied to the entire dataset of GrIS runoffs; this number is therefore speculative and was included for reference only.
‡From ref. [37]. Areal yields are for entire catchment areas, whereas diffusive fluxes refer to stream surface areas.

Extended Data Table 2 | Stable-isotope details for CH_4 and CO_2

Sampling Time	$\delta^{13}C$-CH_4 (‰ VPDB)	$\delta^{2}H$-CH_4 (‰ VSMOW)	$\delta^{13}C$-CO_2 (‰ VPDB)
2015-05-04 12:00	-48.9	-	-16.9
2015-05-04 12:00	-46.1	-	-18.4
2015-05-30 11:30	-6.1	-	-12.2
2015-06-07 12:00	-61.3	-303	-15.3
2015-06-07 12:00	-53.1	-281	-16.0
2015-06-17 23:00	-56.7	-313	-15.8
2015-06-17 23:00	-55.2	-256	-14.5
2015-06-21 16:15	-59.3	-235	-22.2
2015-06-21 16:15	-57.6	-289	-24.1
2015-06-25 15:40	-63.4	-308	-14.6
2015-06-25 05:20	-56.6	-302	-14.8
2015-06-26 18:15	-60.2	-272	-23.6
2015-07-01 09:55	-55.9	-318	-26.8
2015-07-01 09:30	-55.2	-262	-26.2

The first three rows correspond to samples collected at the borehole and the chainsawed hole (see Supplementary Information 1b, Extended Data Fig. 3).

Extended Data Table 3 | Site-specific parameters applied in the one-dimensional hydrate model

Symbol	Parameter	Value	Unit
z_{xn}	Sediment thickness	20-100	m
h	Ice thickness	1,000	m
G	Geothermal gradient	0.025	°C m^{-1}
T(0)	Basal Temperature	-1	°C
sed	Sedimentation rate	0	m s^{-1}
vup	Upward fluid flux	0	m s^{-1}
φ0	Porosity	0.6	-
R_{xn}	Constant methane production rate	10^{-17} - 10^{-13}	g-CH_4 g^{-1} wet-sediment s^{-1}